

# Role of grain boundaries in magma migration and storage

Saswata Hier-Majumder <sup>\*</sup>, Yanick Ricard <sup>1</sup>, David Bercovici

*Department of Geology and Geophysics, Yale University, New Haven, CT, USA*

Received 13 December 2005; received in revised form 18 May 2006; accepted 8 June 2006

Available online 26 July 2006

Editor: C.P. Jaupart

## Abstract

We employ a continuous theory of two-phase flow to investigate the influence of grain boundary tension on distribution and migration of melts through a viscous matrix. The ‘disaggregation melt fraction’, the volume fraction of partial melt at which grain boundaries are completely wetted, is crucial in determining the total interfacial force per unit volume. In partially molten aggregates with small dihedral angles and containing less melt than the disaggregation fraction, capillary action on grain boundaries tends to retain melt in tubules along triple grain junctions. As a consequence, pulses of buoyant magma decay during their ascent through the mantle. Strong interfacial tension on matrix grain boundaries also influences the thickness of a heavy partially molten layer. In aggregates with large dihedral angles, strong tension on grain–melt interfaces can give rise to self-separation of the melt from the matrix.

© 2006 Elsevier B.V. All rights reserved.

*Keywords:* two-phase flow; partial melting; nonlinear waves; magma transport; grain boundary wetting

## 1. Introduction

Migration and storage of melts play critical roles in the thermal and chemical evolution of planetary interiors. Mass and heat transport at mid-oceanic ridges, plumes and volcanic arcs depends on the efficiency of melt extraction from the source region. Melt-rich regions in the mantle act as reservoirs of incompatible elements. Due to the lower viscosity [1] relative to the unmelted silicates, such partially molten boundary layers also play a significant role in long-term stability of mantle plumes [2]. Melts flow along interconnected networks of tubules

and sheets within a viscously deforming matrix [3–6]. Such coupled motion of the melt and the viscous matrix in partially molten aggregates is controlled by a balance between gravity, viscous stresses, pressures, and interfacial tension on the grain–grain and grain–melt interfaces.

Interfacial tension on grain boundaries (grain–grain interfaces) and grain–melt interfaces in partially molten rocks influences the dynamics of melt migration in two ways. First, shape and connectivity of network-forming tubules and sheets of melts along grain edges and boundaries are controlled by the dihedral angle which depends on the ratio between the surface tension on grain–grain and grain–melt interfaces [7–10]. Second, total tension on both grain–grain and grain–melt interfaces balances pressure, viscous drag, and gravitational forces during coupled flow of the matrix and the melt [11–14]. While geometry of the network components is important in establishing a pathway for porous

<sup>\*</sup> Corresponding author. Now at Department of Geology, University of Maryland. Tel.: +1 301 405 6979.

*E-mail address:* [saswata@umd.edu](mailto:saswata@umd.edu) (S. Hier-Majumder).

<sup>1</sup> Also at: Laboratoire de Science de la Terre, Ecole Normale Supérieure de Lyon, Lyon, France.

flow of the melt [7,8], interfacial tension leads to phenomena such as self-separation [11–13] and redistribution [14–16].

A number of previous studies have examined each aspect of interfacial tension on two-phase dynamics separately. The influence of interfacial tension on the geometry of pore fluid networks, melt segregation, and melt redistribution has been investigated in two-phase aggregates under a hydrostatic condition of stress, both experimentally [15–18] and theoretically [3,7,11–14]. Experimental work has demonstrated a strong influence of the grain–grain interfacial tension on melt redistribution [15,16]. However, due to the small length scales of the experimental samples, buoyancy effects were negligible compared to interfacial tension effects. Theoretical work on two-phase flow demonstrated that interfacial tension gives rise to either self-separation or redistribution [3,11–14] of melt. In these analyses the total interfacial tension is treated as a continuous function of the melt fraction, whose effect vanishes in the absence of melts. While such a description is realistic for a mixture of two immiscible liquids, it does not incorporate tension on grain–grain interfaces and its influence on the melt geometry.

In this work, we present a new formulation that directly incorporates the influence of melt geometry on two-phase flow at large length scales. We employ a simple geometric model described in Appendix A to define the total interfacial tension in terms of the semidihedral angle of grain edge tubules. In our model, the melt geometry and total interfacial tension depend on the volume fraction of partial melt. Below a critical melt fraction the melt resides in tubules along grain edges and wets a fraction of the grain boundaries (grain–grain interfaces). We refer to this critical melt fraction as the ‘disaggregation melt fraction’, since the matrix disaggregates at melt fractions greater than or equal to this melt fraction and grain boundaries are completely wetted.

The results indicate that a remarkable difference exists between the behaviors of low dihedral angle aggregates containing partially and completely wetted grain boundaries.

## 2. Formulation

We consider a solid–melt aggregate containing a small fraction of melt, residing primarily in a network of interconnected tubules along triple grain junctions and grain edges. We assume no mass exchange (melting or solidification) takes place between the solid matrix and the melt [19]. Throughout the rest of the paper, we will

use the subscripts f and m to indicate the fluid (partial melt) and the viscous solid matrix, respectively.

Interfacial force in a two-phase aggregate is related to the interfacial area per unit of the control volume. Since the interfacial area is averaged over a control volume containing several grains and melt pockets and yet not large enough to exhibit any significant variation of the field variables, the location and geometry of the interfaces within the control volume remain unknown [11]. When only one interface separates two different phases (i.e. only the matrix–fluid interface is present), the interfacial force can be expressed as  $\sigma\alpha$ , where  $\sigma$  is a temperature dependent surface tension and  $\alpha$  is the interfacial area density, dependent only on the volume fraction of one of the phases,  $\phi$  [11]. One important property of  $\alpha$  is  $\alpha \rightarrow 0$  as  $\phi \rightarrow 0, 1$ ; corresponding to each individual phase constituting the entire aggregate. However, in a viscous, polycrystalline matrix, the presence of grain boundaries requires  $\alpha \neq 0$  when the melt volume fraction  $\phi = 0$ . To address this issue, we express the total interfacial tension as a sum of the interfacial forces on the solid–solid interfaces (grain boundaries) and solid–liquid (grain–melt) interfaces. This quantity is described as  $\chi = \sigma_{mm}\alpha_{mm} + \sigma_{mf}\alpha_{mf}$ , where subscript ‘mm’ indicates matrix–matrix (grain–grain) and ‘mf’ indicates matrix–fluid (grain–melt) interfaces. Next, in order to define a functional form of  $\chi$ , we use a simple representative geometric model within a control volume described in Appendix A. We also demonstrate that such an approach does not violate the fundamental energy conservation rules in Appendix B. Essentially, this approach treats the grain–grain interfaces as a limiting case of two grain–melt interfaces, placed an infinitesimally small distance away, separated by an infinitesimally thin melt film.

### 2.1. General governing equations

Consider a partially molten aggregate containing a spatially and temporally variable melt fraction  $\phi$ . In this aggregate, both the solid matrix and the melt flow as viscous fluids with viscosities  $\mu_m$  and  $\mu_f$ , while their respective velocities are given by the quantities  $v_m$  and  $v_f$ . The densities of the matrix and the fluid phases are given by  $\rho_m$  and  $\rho_f$ , respectively. We treat the pressures of the matrix and the fluid as independent quantities given by  $P_m$  and  $P_f$ .

The mass conservation equations for both phases are given by:

$$\frac{\partial \phi}{\partial t} + \nabla \cdot (\phi v_f) = 0, \quad (1)$$

$$\frac{\partial(1-\phi)}{\partial t} + \nabla \cdot ((1-\phi)\mathbf{v}_m) = 0. \quad (2)$$

We also assume that the fluid viscosity is negligible compared to the matrix viscosity ( $\mu_f=0$ ), in which case the interfacial forces are supported entirely by the matrix [20]. Under this condition, the momentum equation for each individual phase is given by [11,20]:

$$0 = -\phi(\nabla P_f + \rho_f g \hat{\mathbf{y}}) + c\Delta \mathbf{v}, \quad (3)$$

$$0 = -(1-\phi)(\nabla P_m + \rho_m g \hat{\mathbf{y}}) - c\Delta \mathbf{v} + \nabla \cdot ((1-\phi)\underline{\boldsymbol{\tau}}_m) + \left(\frac{\partial \chi}{\partial \phi} + \Delta P\right) \nabla \phi, \quad (4)$$

where  $\Delta q = q_m - q_f$  for any quantity  $q$ . The interaction coefficient  $c$  arises from viscous interaction at the fluid–matrix interface and is inversely proportional to the permeability ([11], see also Section 2.4).

The constitutive relation for the matrix is given by,

$$\underline{\boldsymbol{\tau}}_m = \mu_m \left( \nabla \mathbf{v}_m + [\nabla \mathbf{v}_m]^t - \frac{2}{3} \nabla \cdot \mathbf{v}_m \underline{\mathbf{I}} \right). \quad (5)$$

The stress drop condition, as derived in Appendix B, is:

$$\frac{\partial \chi}{\partial \phi} + \Delta P = -\frac{K_0 \mu_m}{\phi(1-\phi)} \frac{Dm}{Dt}, \quad (6)$$

where  $K_0$  is a dimensionless constant of  $O(1)$  and the material derivative  $D_m/Dt$  is given by:

$$\frac{Dm}{Dt} = \frac{\partial}{\partial t} + \mathbf{v}_m \cdot \nabla. \quad (7)$$

The quantities on the left hand side of Eq. (6) arise from gradient of interfacial tension and the pressure drop across matrix–melt interfaces. The quantity on the right hand side arises from compaction of the matrix (see details in Appendix B). Eq. (6) indicates that departure from surface tension equilibrium is driven by compaction of the aggregate.

To close the system of Eqs. (1)–(6), an additional phenomenological relation between  $\chi$  and one of the unknowns is necessary. Notice that the quantity  $\partial \chi / \partial \phi$  in Eqs. (4) and (6) appear as  $\sigma(\partial \alpha) / (\partial \phi)$ , in the formulation given in [11], in which only interfacial tension arising from the solid–liquid interface is considered. At fluid volume fractions less than the disaggregation melt fraction, both the grain–grain and grain–melt interfacial tensions contribute to  $\chi$ . At the disaggregation melt fraction, the grain boundaries are completely wetted, and the only interface present is the

solid–liquid interface. As the simple geometric derivation in Appendix A indicates, the relationships between  $\chi$  and  $\phi$  below and above the disaggregation melt fraction are given by:

$$\chi(\phi) = \begin{cases} \alpha_0 [\sigma_{mf} \chi_1 \sqrt{\phi} + \sigma_{mm} (1 - \chi_2 \sqrt{\phi})] & \text{if } \phi < \phi_s, \\ \sigma_{mf} \alpha_0 \sqrt{\pi(1-\phi)} & \text{if } \phi \geq \phi_s, \end{cases} \quad (8)$$

where  $\chi_1$  and  $\chi_2$  are parameters dependent on  $\theta$ , the semidiagonal angle, the angle subtended by the grain–melt interface to the grain boundary (see Fig. A.1). The semidiagonal angle  $\theta$  controls the geometry of the melt network, as indicated in the micromechanical model in Appendix A. The quantity  $\alpha_0$  is the reciprocal of the average grain size and  $\phi_s$  is the disaggregation melt fraction. Although in this work we employ a relatively simple model of melts along the grain boundaries, very similar results are obtained from analyses with a tetrakaidecahedral geometry of the solid grains [8].

The forces governing the conservation of momentum of two-phase aggregates are proportional to the gradients of matrix and fluid pressures as evidenced in Eqs. (3) and (4). While the first derivative of  $\chi$  with respect to  $\phi$ ,  $\chi'$ , is proportional to the difference between matrix and fluid pressures, as evidenced in Eq. (6), the second derivative  $\chi''$  is proportional to the difference between matrix and fluid pressure gradients and indicates the gradient of total interfacial tension. When  $\chi''$  is positive, the interfacial force tends to drive melt into low pressure regions by capillary action. This takes place in a partially molten aggregate with a low dihedral angle, caused by a stronger grain–grain interfacial force compared to the grain–melt interfacial force. Fig. 1 depicts  $\chi$  and  $\chi''$  as a function of  $\phi$  for two such cases for semidiagonal angles of  $60^\circ$  and  $0^\circ$ . Although in an aggregate with a zero dihedral angle, grain boundaries are completely wetted, we consider  $\phi \rightarrow 0^\circ$  as a positive, vanishingly small dihedral angle to demonstrate the maximum influence of grain boundary tension. In the curve for  $\phi \rightarrow 0^\circ$ , interfacial tension on grain boundaries is the maximum as allowed by the scenario described in Appendix A, and  $\chi''$  is positive for melt fractions below the disaggregation melt fraction. For  $\phi = 60^\circ$ , as well as for melt fractions greater than the disaggregation melt fraction,  $\chi'' < 0$ , indicating that the surface tension attracts melts into the region of high melt pressure.

## 2.2. Coalescence

In general, the function  $\chi(\phi)$  and its derivatives display a discontinuity at the disaggregation melt

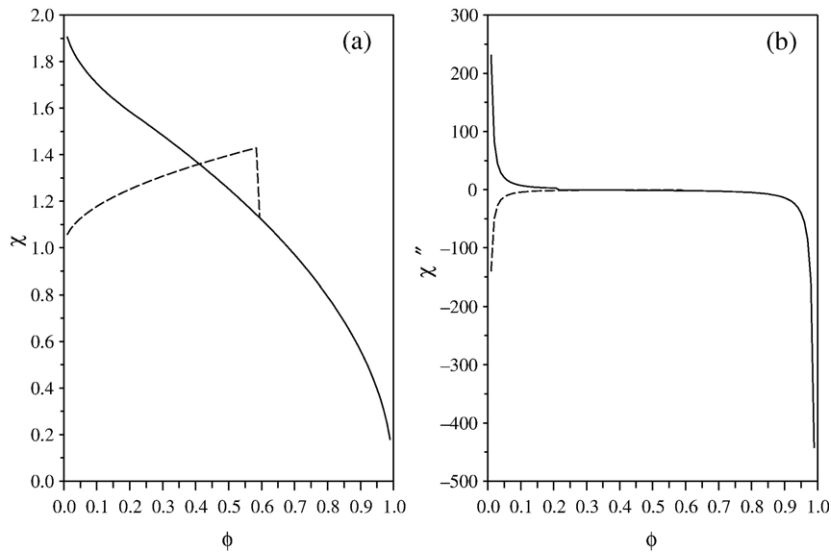


Fig. 1. Plots of total surface tension  $\chi$  and  $\chi''$  as a function of  $\phi$ . The solid and broken curves correspond to  $\theta \rightarrow 0^\circ$  and  $\theta = 60^\circ$ , respectively. The disaggregation melt fraction,  $\phi_s$ , for  $\theta \rightarrow 0^\circ$  and  $\theta = 60^\circ$  is 0.21 and 0.59, according to Eq. (A.9) in Appendix A.

fraction, as evidenced in the plots in Fig. 1. The discontinuity arises due to a change in the surface curvature and surface tension of the nontouching, spherical grains to contiguous, faceted grains during coalescence by a process known as ‘contact flattening’ [21,22]. As the surfaces of two approaching spherical grains reach a critical separation distance, short range forces start to dominate [23]. As the grains continue approaching each other beyond the critical separation, driven by the short range forces, they deform in a viscous manner until the separation becomes comparable to intermolecular distance and the area of contact becomes flat [24]. Thus, the process of contact flattening by viscous deformation of the grains is essentially continuous and involves large deformation of the grain–melt interface over a very small range of melt fraction. Apart from the shape and surface area of the grains, the surface tension also changes during coalescence. With decreasing separation, tension on two isolated grain–melt interfaces changes continuously into the tension of one flat grain–grain interface in the region of contact [23]. As a combination of changes in surface area and surface tension, small fluctuations in  $\phi$  induce large changes in  $\chi$  near the disaggregation melt fraction. Thus, the discontinuity in  $\chi$  in our present formulation stems from phenomena at the very small length scales.

Due to the viscous nature of deformation, complete description of shape change by contact flattening during coalescence requires knowledge of the velocity, pressure drop, and surface tension at the interfaces. A detailed solution for the shape evolution of coalescing grains is

beyond the scope of this article. However, our present macroscopic, geometric description given in Appendix A provides an adequate first order approximation.

We ran a number of tests to assess the influence of the discontinuity on the end result. First we used a filter to smooth the discontinuity in  $\chi$  and its derivatives in Eq. (8). Next, we used the smoothed function in our codes to solve for melt fraction and velocity. Finally, we compared the melt and velocity distribution obtained by using the smoothed function with those obtained by using Eq. (8). The melt and velocity distribution from both runs agreed remarkably well, indicating that the discontinuity in  $\chi$  did not influence the final results.

### 2.3. One-dimensional equations

In this work we solve the system of Eqs. (1)–(6), along with the interfacial tension relation (8) in one-dimension in a domain of length  $2l$ . To arrive at the one-dimensional equations, we take the general governing Eqs. (1)–(6), and consider the case where the only nonzero motion and gradients are along the vertical ( $y$ ) direction. The boundary conditions for the velocities of both phases are given by,

$$v_m = v_f = 0 \text{ at } y = \pm l \quad (9)$$

and the initial melt distribution is,

$$\phi(y, 0) = \phi_0(y). \quad (10)$$

The sum of the mass conservation Eqs. (1) and (2), combined with boundary conditions for vertical velocities yields

$$\phi v_f + (1-\phi)v_m = 0. \quad (11)$$

The equation for mass conservation of the matrix yields,

$$\frac{\partial \phi}{\partial t} = \frac{\partial}{\partial y} ((1-\phi)v_m). \quad (12)$$

We can eliminate the pressures of the individual phases by combining Eqs. (3) and (4), to obtain the action-reaction equation given by,

$$0 = (1-\phi)\chi'' \frac{\partial \phi}{\partial y} + \frac{\partial}{\partial y} \left( \mu_m \left( \frac{K_0}{\phi} + \frac{4}{3} \right) (1-\phi) \frac{\partial v_m}{\partial y} \right) - (1-\phi)\Delta\rho g - \frac{c v_m}{\phi^2} \quad (13)$$

By solving Eqs. (12) and (13), all unknowns can be determined.

#### 2.4. Nondimensionalization

We nondimensionalize velocity, length, and surface tension according to the relations:

$$v_m = \frac{\rho_m g \delta_m^2}{\mu_m} w^*, \quad y = \delta_m y^*, \quad \chi = \sigma_{mf} \alpha_0 \chi^*. \quad (14)$$

The length scale used in the nondimensionalization is the matrix compaction length  $\delta_m = \sqrt{(4\mu_m)/(3c)}$ . Also, adding the constraint  $K_0=4/3$ , Eqs. (12) and (13) can be nondimensionalized into

$$\frac{\partial \phi}{\partial t} = \frac{\partial}{\partial y} ((1-\phi)w) \quad (15)$$

$$0 = \xi(1-\phi)\chi'' \frac{\partial \phi}{\partial y} + \frac{4}{3} \frac{\partial}{\partial y} \left( \frac{(1-\phi^2)}{\phi} \frac{\partial w}{\partial y} \right) - R(1-\phi) - \frac{4}{3} \frac{w}{\phi^2}, \quad (16)$$

where the asterisks have been dropped off the nondimensional variables. The nondimensional constants are given by,

$$\xi = \frac{\sigma_{mf} \alpha_0}{\rho_m g \delta_m}, \quad R = \frac{\Delta\rho}{\rho_m}. \quad (17)$$

The compaction length  $\delta_m$  depends on the matrix viscosity  $\mu_m$  and the interaction coefficient  $c$ . For

negligibly small viscosity of the melt, the interaction coefficient  $c = \mu_f \phi^2 / k_p$ , where  $k_p$  is the permeability ([11], Section 4.3). Employing a simple model of melt percolation through tubules along grain edges, one obtains  $k_p = \phi^2 / 72\pi\alpha_0^2$ , where  $1/\alpha_0$  is the grain size ([25], Section 9.3). Thus we obtain  $c \approx 10^{10} \text{ Pa s m}^{-2}$ , for a melt viscosity  $\mu_f = 1 \text{ Pa s}$  and a grain size  $1/\alpha_0 = 100 \text{ }\mu\text{m}$ . This corresponds to a matrix compaction length  $\delta_m = 10 \text{ km}$ , for a matrix viscosity  $\mu_m = 10^{18} \text{ Pa s}$ . We have also used  $\Delta\rho = 300 \text{ kg m}^{-3}$  and  $\rho_m = 3 \times 10^3 \text{ kg m}^{-3}$ , leading to  $R = 0.1$ . The interfacial tension  $\sigma_{mf} = 1 \text{ J m}^{-2}$  [26]. The selection of the parameters implies that for  $\xi = 10^{-4}$ , nondimensional unit matrix velocity and time are equivalent to dimensional matrix velocity and time of  $3 \times 10^{-6} \text{ m s}^{-1}$  ( $\approx 100 \text{ m yr}^{-1}$ ) and  $3.3 \times 10^9 \text{ s}$  ( $\approx 100 \text{ yr}$ ), respectively. In this work we examine the influence of surface tension in the numerical experiments by using different values of  $\xi$  between  $10^{-6}$  and  $10^{-2}$ .

### 3. Results

We employ Eqs. (15) and (16) to solve for the matrix velocity  $w$  and the melt fraction  $\phi$ . We obtain an analytical solution for the linearized form of Eq. (13), while the complete nonlinear equation is solved numerically using the finite volume method with an explicit time marching scheme. The numerical solutions for self-separation in the absence of gravity were obtained for a zero velocity boundary condition (i.e. velocity of both phases are zero at the top and the bottom). The solutions in the presence of gravity are obtained for a periodic boundary condition. Finally, we obtain a similarity solution to the nonlinear equations in the absence of surface tension as outlined in Appendix C.

#### 3.1. Marginal stability analysis

We linearize Eqs. (15) and (16), by adding small perturbations  $\phi_1(y, t)$  and  $w_1(y, t)$  to constant background values  $\phi_0$  and  $w_0$ . The dependent variable  $\chi$  can be expressed by a Taylor series expansion near the background value. Thus, the variables in the perturbed state are given by,

$$\phi = \phi_0 + \epsilon\phi_1, \quad w = w_0 + \epsilon w_1,$$

$$\chi = \chi(\phi_0) + \epsilon\chi'_0\phi_1, \quad \chi' = \chi'_0 + \epsilon\chi''_0\phi_1, \quad (18)$$

where  $\chi'_0 = \chi'(\phi_0)$ . In order to determine the background melt fraction and velocity, we replace the perturbed

variables from Eq. (18) into Eqs. (15) and (16). Dropping the subscript 1, and dropping terms containing the second or higher powers of  $\epsilon$ , we obtain the linearized equations,

$$\frac{\partial w}{\partial y} = \frac{1}{1-\phi_0} \left( \frac{\partial \phi}{\partial t} + w_0 \frac{\partial \phi}{\partial y} \right), \quad (19)$$

$$0 = \epsilon \left[ \xi(1-\phi_0)\chi_0'' \frac{\partial \phi}{\partial y} + \frac{4}{3} \left( \frac{1+\phi_0}{\phi_0} \right) \left( \frac{\partial^2 \phi}{\partial t \partial y} + w_0 \frac{\partial^2 \phi}{\partial y^2} \right) + R\phi - \frac{4}{3} \left( \frac{w}{\phi_0^2} - 2 \frac{w_0 \phi}{\phi_0^3} \right) \right] - R(1-\phi_0) - \frac{4}{3} \frac{w_0}{\phi_0^2}, \quad (20)$$

which yield on the zeroth order

$$w_0 = -\frac{3R}{4} \phi_0^2 (1-\phi_0). \quad (21)$$

We take  $O(\epsilon)$  equations and substitute  $\phi$  of the form

$$\phi_1 = \tilde{\phi} \exp(st) \exp i(ky - \omega t), \quad (22)$$

yielding a growth rate  $s$ , of perturbations,

$$s = -\frac{3\xi\chi_0''\phi_0^2(1-\phi_0)^2k^2}{4(1+\phi_0(1-\phi_0^2)k^2)}. \quad (23)$$

The dispersion relation between the frequency and the wavenumber is given by,

$$\omega = -\frac{3Rk}{4} \phi_0(1-\phi_0) \left( \frac{(2-3\phi_0)}{1+\phi_0(1-\phi_0^2)k^2} - \phi_0 \right). \quad (24)$$

The dispersion relation (24) leads to the phase and group velocities  $U_{ph} = \omega/k$  and  $U_g = \partial\omega/\partial k$ , respectively.

Growth rate of perturbations is strongly influenced by the presence of grain boundaries. The plots in Fig. 2 (a) illustrate that perturbations of all length scale (indicated by the wave number  $k$ ) grow into instabilities when  $\phi_0 > \phi_s$  and decay into a homogeneous distribution when  $\phi_0 < \phi_s$ , as indicated by the sign of the growth rate. For a given perturbation, growth rate also depends on the semidihedral angle  $\theta$ . The curves in Fig. 2(b) indicate that when  $\theta \rightarrow 0^\circ$ , perturbations can either decay or grow depending on whether the background melt fraction is less or more than  $\phi_s$ . In an aggregate with  $\theta = 60^\circ$ , the same perturbation always grows into an instability.

The quantity  $\chi''$ , which controls the sign of the growth rate, is proportional to the gradient of surface

tension forces. A positive value of  $\chi''$  implies that the total interfacial force drives melt into low pressure regions resulting in homogenization, whereas a negative value indicates that the interfacial force attracts melt from low pressure into high pressure region leading to an instability. According to the model in Appendix A, strong interfacial tension on grain boundaries leads to small dihedral angles and thus renders the quantity  $\chi''$  positive. For weak grain boundary tension and large dihedral angles,  $\chi''$  is always negative, and a self-separation like behavior is observed.

### 3.2. Nonlinear analysis

In this section we present solutions to the nonlinear Eqs. (15) and (16). We discuss the influence of grain boundary wetting in the evolution of melt perturbations in the absence of gravity in Section 3.2.1 and demonstrate the simultaneous influence of grain boundary wetting and gravity on ascending melt perturbations in Section 3.2.2.

#### 3.2.1. Surface tension under neutrally buoyant conditions

In the absence of gravitational force and deformation, the surface tension forces are balanced by the pressure difference between the solid and the fluid phases and the viscous drag at the grain–melt interface. Figs. 3–5 demonstrate the evolution of an initial perturbation in melt distribution with time. In all three of these plots, the length of the domain is equal to twice the compaction length of the matrix. While values of parameters  $R$  and  $\xi$  are 0 and  $1 \times 10^{-3}$ , semidihedral angle  $\theta \rightarrow 0^\circ$  for all three plots, respectively.

The plot of melt distribution at several time steps depicted in Fig. 3(a) illustrates surface tension driven self-separation of the melt. In this case the initial melt distribution is given by a Gaussian perturbation with a background value larger than the disaggregation melt fraction. Under such a condition, no grain boundaries are present and the result is similar to that obtained by previous works [12,13,20]. The initial perturbation containing a peak of 40 vol.% melt grows into a wider perturbation containing 55 vol.% melt at its peak. The time evolution of the matrix velocity depicted in Fig. 3 (b) demonstrates that the matrix velocity is always fastest at the flank of the perturbation, corresponding to the steepest gradient in the melt distribution.

Consequently, melt gets drained through these regions most quickly, as seen in Fig. 3(a). Also, positive value of the matrix velocity above the perturbation and negative matrix velocity below the perturbation

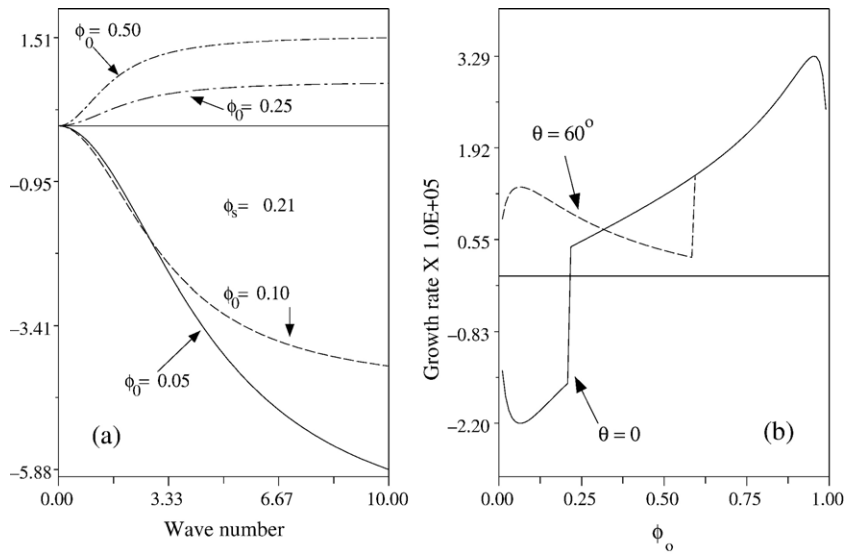


Fig. 2. Results from the linear analysis for  $\xi=1 \times 10^{-4}$  and  $R=0.1$ . (a) Growth rate of melt perturbations as a function of nondimensionalized wavenumber. Each curve corresponds to a different value of melt fraction in the unperturbed state marked in the plots. (b) Growth rate as a function of the background melt fraction  $\phi_0$ , for wavenumber  $k=3$ . The broken curve corresponds to  $\theta=60^\circ$ , while  $\theta \rightarrow 0^\circ$  for the solid curve.

indicates that the matrix decompacts accommodating for the flow of melt into the perturbation. Notice also, with increasing time, the width of the melt-rich region increases.

The pattern of melt segregation is remarkably different when the background melt fraction is below the disaggregation melt fraction and the peak melt fraction

above the disaggregation melt fraction (Fig. 4(a) and (b)). In Fig. 4(a) the background region remains almost undrained while the initial perturbation becomes narrower as it grows at its own expense. As revealed in the plot of velocity distribution in Fig. 4(b), the matrix velocity is still highest at the flanks of the initial perturbation. However, with time the melt from the flank is drained into the peak

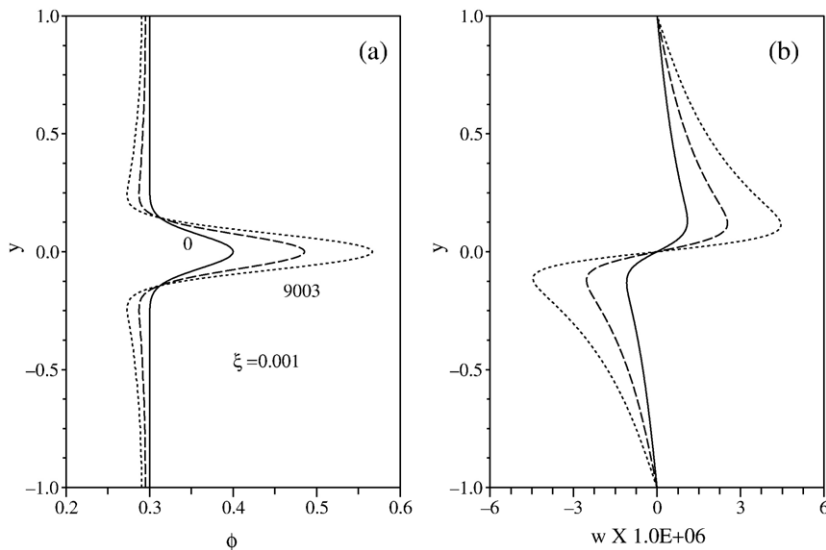


Fig. 3. Self-separation of the melt driven by grain–melt interfacial tension. (a) Melt fraction as a function of depth. The initial background melt fraction is larger than the disaggregation melt fraction, indicating the presence of only the grain–melt interface. (b) Matrix velocity as a function of depth. The matrix velocity is positive just above the perturbation and negative just below, indicating decompaction near the center as melt self-separates. The numbers adjacent to the initial (solid lines) and final (finely dashed lines) profiles indicate corresponding nondimensional times.

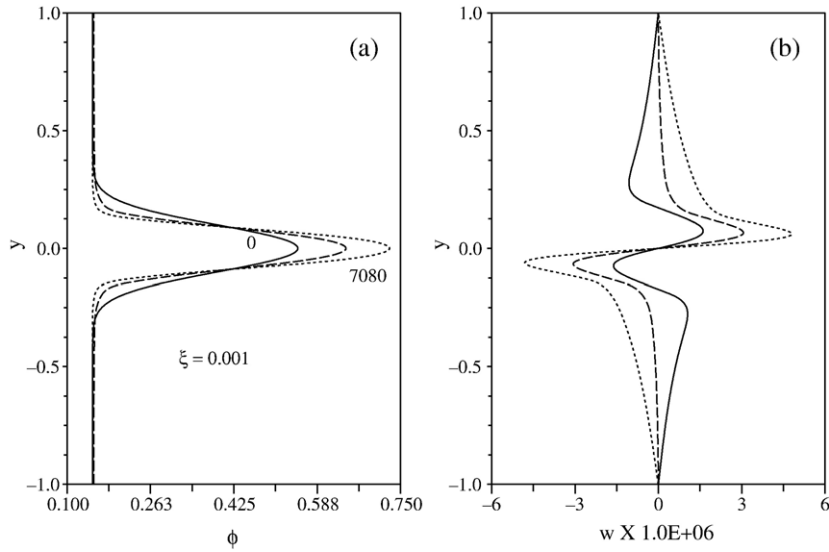


Fig. 4. Simultaneous homogenization and self-separation. The background melt fraction is below the disaggregation melt fraction and remains mostly unchanged. (a) Melt fraction as a function of depth. The initial perturbation grows into a narrower, but larger perturbation with time. (b) Matrix velocity as a function of depth. Distribution of the matrix velocity indicates that matrix moves away from the center as the perturbation draws more melt towards the center. The numbers adjacent to the initial (solid lines) and final (finely dashed lines) profiles indicate corresponding nondimensional times.

of the perturbation causing the perturbation to shrink in width. The most important feature in this case is the extremely slow melt extraction from the background. Since the background melt fraction is below the critical limit, a fraction of the grain boundaries in these regions

are unwetted and their interfacial tension hinders melt extraction from the background. This behavior contrasts with the observation from previous formulations where it was possible to completely drain the matrix in the absence of grain boundaries [12,13,20].

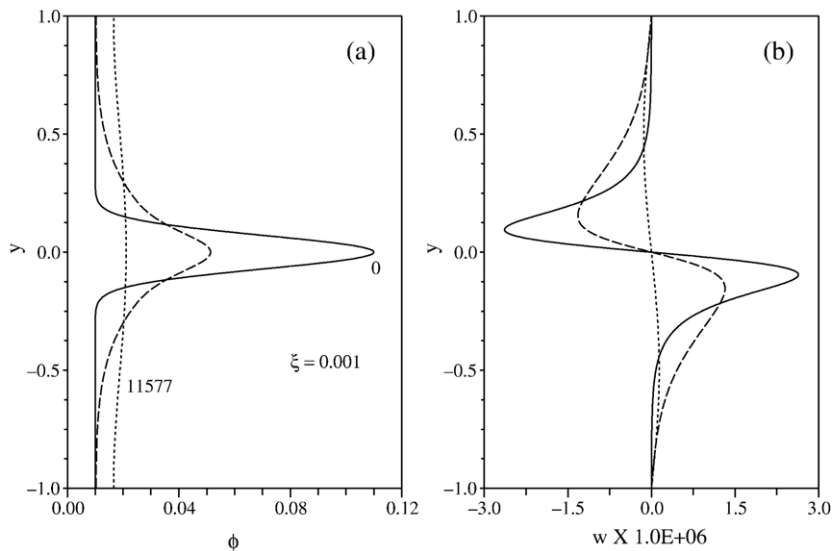


Fig. 5. Homogenization of the melt perturbation by grain boundary wetting. (a) Melt fraction as a function of depth. The initial perturbation homogenizes to a uniform distribution. (b) Matrix velocity as a function of depth. The matrix velocity is negative just above the perturbation and positive just below the perturbation, implying advection of the matrix towards the center as the melt moves away from the center. The numbers adjacent to the initial (solid lines) and final (finely dashed lines) profiles indicate nondimensional times corresponding to the profiles.



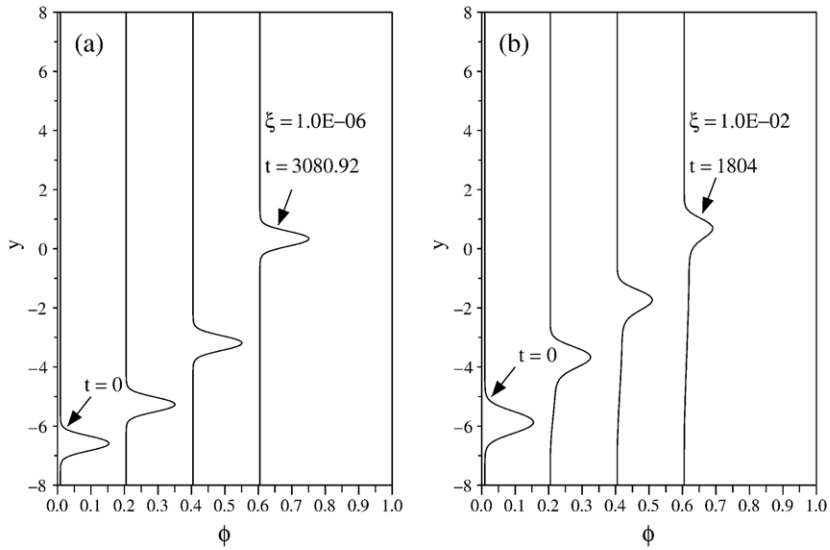


Fig. 6. Successive plots of melt fraction as a function of depth displaying the influence of grain–grain interfacial tension on melt retention. In panel (a), tension on grain–grain interfaces is negligible compared to gravity and the solitary melt pulse travels undisturbed. In panel (b), large value of  $\xi$  due to tension on grain–grain interfaces retains melt in the matrix column during the ascent of the melt pulse.

Perturbations in melt distribution are rapidly homogenized by grain boundary wetting when both the peak and background melt fractions are less than the disaggregation melt fraction, as illustrated in Fig. 5(a). Notice that the distribution of matrix velocity in Fig. 5 (b) is opposite to the previous two cases, indicating the matrix compacts at the perturbation as the melt diffuses

out. The homogenization of the perturbation can be compared to the situation described in the linear analysis. In the linear analysis, we have demonstrated that the growth rate of the perturbations becomes negative for melt fractions below the disaggregation melt fraction. Such diffusive redistribution of basaltic melts driven by grain–grain interfacial tension of

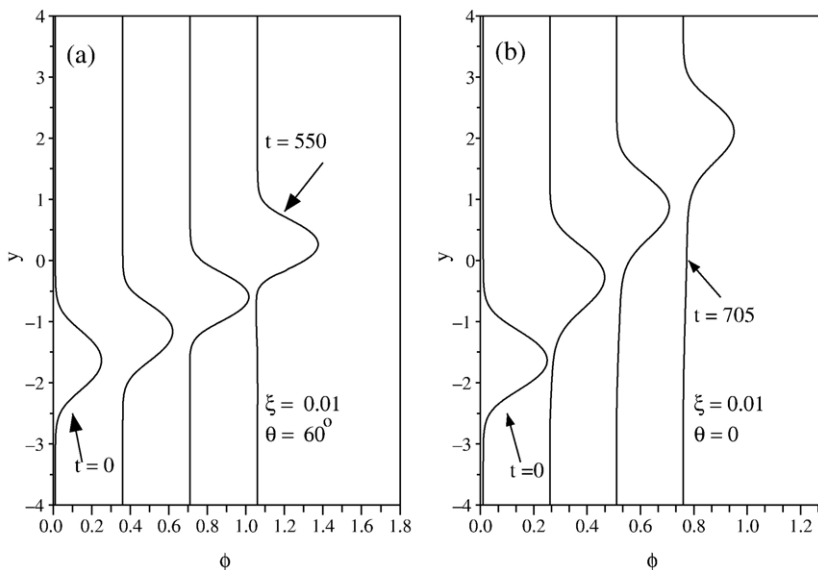


Fig. 7. Successive plots of melt fraction as a function of depth demonstrating ascent of two solitary magma packets. For both plots  $\xi=0.01$ ,  $R=0.1$ . (a)  $\theta=60^\circ$  and (b)  $\theta \rightarrow 0^\circ$ . The amplitude of the solitary wave increases during ascent in (a) while it decreases in (b).

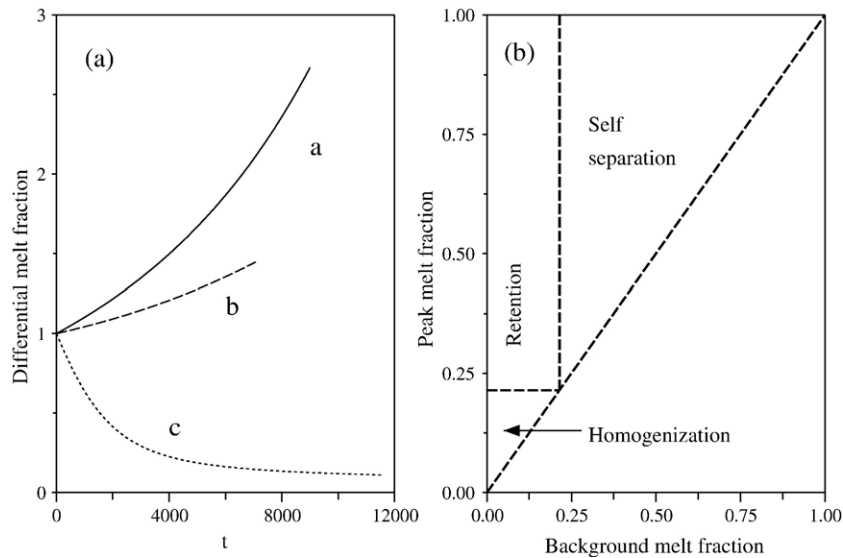


Fig. 8. (a) Plot of normalized differential melt fraction  $(\phi_{\max} - \phi_0)/(\phi_{\max} - \phi_0)_{t=0}$  as a function of time. The curves marked 'a', 'b', and 'c' correspond to the cases presented in Figs. 3, 4, and 5, respectively. The peak melt fraction increases for the first two cases while it decreases with time for the third case. (b) Regime diagram for self-separation (Fig. 3), melt retention (Fig. 4), and homogenization (Fig. 5) as a function of background melt fraction ( $\phi_0$ ) and peak melt perturbation ( $\phi_m$ ). Since the background is defined to be less than or equal to the peak perturbation, no realistic solution exists in the lower right half of the plot. The disaggregation melt fraction corresponds to the case of  $\theta \rightarrow 0$ .

silicate minerals has also been experimentally observed in aggregates with small grain size and much smaller length scale [15,16].

### 3.2.2. Surface tension and gravity

Gravitational instability leads to compaction of partially molten columns of rock, generating solitary magma pulses or 'magmons' [27]. Magmons are soliton solutions to the governing equations for two-phase flow. In the absence of surface tension, an individual magmon ascends through a column of rocks with a constant amplitude [27–31]. Strong surface tension, however, leads to dissipation and the amplitude of the magmons changes during their ascent [12]. In this section, we discuss the influence of interfacial tension on the amplitude of an ascending magmon, and demonstrate that strong grain–grain interfacial tension leads to partial retention of melt near its source region. To obtain the results in this section we solved Eqs. (15) and (16) using a periodic boundary condition. We also employed the analytical solution presented in Appendix C to calculate the initial magmon shape function.

The surface tension on the grain–grain interfaces influences the evolution of the amplitude of a magmon. Fig. 6 represents two individual magmons with initial background and peak melt fractions of 1 and 15 vol.% s. In Fig. 6(a),  $\xi = 10^{-6}$ , indicating surface tension is negligibly small compared to gravity, whereas in Fig. 6

(b),  $\xi = 0.01$ , indicating the presence of strong surface tension. In both of these cases  $\theta \rightarrow 0^\circ$ . In the absence of surface tension, the magmon rises through the column with a constant amplitude. However, in the presence of strong surface tension forces, the amplitude of the

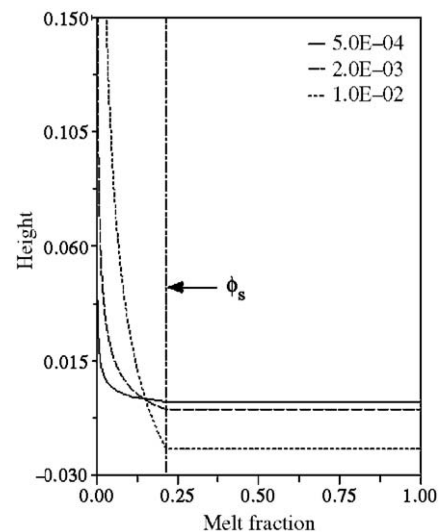


Fig. 9. Steady state distribution of a dense melt layer with  $R = -0.1$ . The curves represent analytical solutions to Eq. (25) for three different values of  $\xi$ . The tension on the grain–melt interface is assumed to be negligibly small compared to the grain boundary tension.

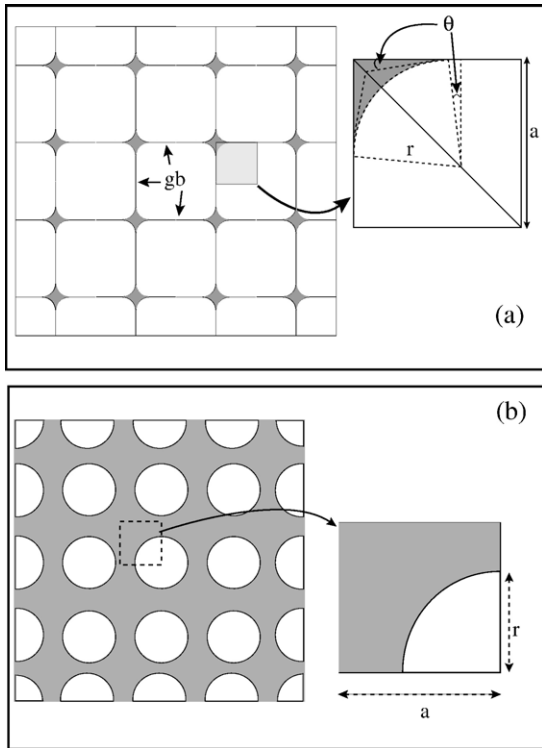


Fig. A.1. Schematic diagram illustrating the face of the control volume for (a) melt fraction less than disaggregation melt fraction, and (b) melt fraction more than disaggregation melt fraction. The angle  $\theta$  is half of the dihedral angle subtended by two solid–liquid interfaces at the junction with a solid–solid interface.

magmon decays during its ascent while melt from the peak of the magmon is drained into the matrix. The magmon is followed by a wake retaining some of the melt. The contrasting behaviors of the magmons in these two cases clearly indicate that in the presence of strong grain–grain interfacial tension, a small amount of melt is retained behind each ascending pulse of buoyant magma.

Contrary to strong grain–grain interfacial tension, strong tension on grain–melt interfaces can lead to self-separation in buoyant magmons. Fig. 7(a) and (b) compares two such cases corresponding to  $\theta=60^\circ$  and  $\theta\rightarrow 0^\circ$ . When  $\theta=60^\circ$ , the magmon exhibits a self-separation like behavior, and melt is drained from the flank into the magmon. As indicated in Fig. 1(b), the second derivative of surface tension, which is proportional to the differential pressure gradient, becomes negative for  $\theta=60^\circ$ , forcing melt to move from low pressure to high pressure. Self-separation of an ascending magmon eventually drains the matrix entirely, and the magmon evolves into a stationary sill, as also observed in previous works [12]. On the contrary, the amplitude of the magmon decays during its ascent when  $\theta\rightarrow 0^\circ$ . Strong capillary tension of the grain boundaries

forces melt to drain away from high pressure regions. Thus, simultaneous homogenization and ascent of the melt give rise to retention of small amounts ( $\sim 1$  vol.%) of melt near the source region.

#### 4. Discussions

##### 4.1. Efficiency of melt extraction

Tension on the grain–grain interfaces suppresses self-separating instabilities and reduces the efficiency of melt extraction. Fig. 8(a) illustrates the normalized differential melt fraction  $(\phi_{\max} - \phi_0)/(\phi_{\max} - \phi_0)_{t=0}$  as a function of time for the three cases ‘a’, ‘b’, and ‘c’ corresponding to Figs. 3, 4, and 5, respectively. In the absence of grain boundaries, the peak melt fraction in curve ‘a’ increases rapidly. On the contrary, capillary action arising from grain–grain interfacial tension drains melt away from the peak in curve ‘c’. Finally, curve ‘b’ displays a slow growth of the differential melt fraction, indicating inefficient draining of the matrix. Strong tension on the grain–grain interfaces results in small dihedral angles and gives rise to a well-connected melt network with high permeability. Therefore, it is tempting to conclude that melt extraction in such aggregates will be favored. However, comparison between curves ‘a’ and ‘b’ indicates that in the presence of grain boundaries, the efficiency of melt extraction from low-dihedral angle aggregates can be reduced.

Three distinct regimes of melt redistribution can be identified in Fig. 8 for a semidihedral angle  $\theta\rightarrow 0$ , where the  $x$  and  $y$  axes represent background and peak melt fractions respectively. When both the peak and the background melt fraction are less than the disaggregation melt fraction, perturbations are homogenized. In the

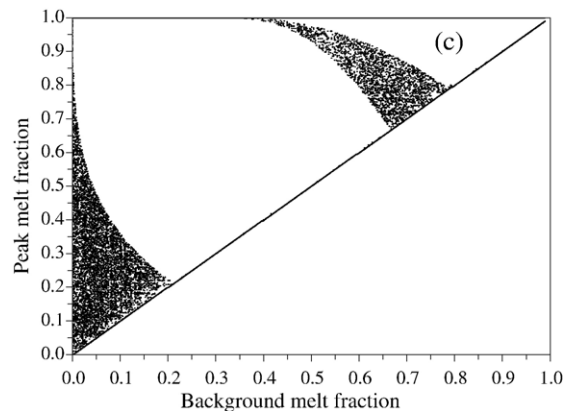


Fig. C.1. Map of solitary wave solution to Eqs. (15) and (16) in the  $\Phi_0 - \Phi_m$  space. The shaded region indicates permissible real solutions. Solutions do not exist in the lower right half of the plot.

absence of grain boundaries (i.e. both background and peak melt fractions are larger than the disaggregation melt fraction), perturbations self-separate and give rise to instabilities. A combination of both processes gives rise to melt retention when the peak perturbation is larger than the disaggregation melt fraction, whereas the background melt fraction is less than the disaggregation melt fraction. We also notice that for very large dihedral angles,  $\chi'' > 0$  for all melt fractions and surface tension always gives rise to self-separation.

#### 4.2. Thickness of dense melt-rich layers

Dense, low viscosity melt-rich layers play a crucial role in thermal and chemical evolution of the mantle. Combined seismic evidence and laboratory measurements suggest the presence of two such layers of variable thickness at the transition zone and the core mantle boundary [2,32–34]. In the zeroth order, the shape of this layer is determined by pooling of the melt at the bottom of the column containing the matrix and the melt. However, capillary tension on the grain boundaries in the matrix can curtail the extent of gravitational settling and give rise to the presence of a boundary layer between the disaggregated layer and the matrix. The overlying aggregate with low melt fraction and high concentration of grain boundaries acts like a sponge and retains melt. In the steady state, negative buoyancy of a dense melt is balanced by the interfacial tension, given by

$$\frac{\partial}{\partial y}(\chi'(\phi)) = \frac{R}{\xi}. \quad (25)$$

The effect of interfacial tension is modulated by the parameter  $\xi$  defined in Eq. (17). Three different normalized solutions to Eq. (25) for  $R = -0.1$  corresponding to three different values of  $\xi$  are plotted in Fig. 9. The interfacial tension on the grain–melt interfaces is negligible compared to the tension on grain–grain interfaces. The thickness of the melt-rich boundary layer is higher for larger values of  $\xi$ , indicating that a larger amount of melt is retained in tubules in the matrix in the presence of a strong interfacial tension, corresponding to a large  $\xi$ .

Two geologically relevant parameters that control the value of  $\xi$  are grain size and the matrix viscosity (through the matrix compaction length). Therefore the steady state thickness of the partially molten boundary layer is also modulated by these two quantities. In the Earth's mantle, orders of magnitude variations in grain size and viscosity can arise from variations in temperature, phase change, or the presence of volatiles. Consequently, the steady state thickness of the dense, melt-rich layers will also show substantial variation corresponding to these variations.

## 5. Conclusion

In conclusion, our results demonstrate that in partially molten aggregates with low dihedral angles, interfacial tension on the grain boundaries controls the melt distribution. Three distinct processes of melt redistribution, self-separation, homogenization, and retention can operate depending on the amount of melt present. Capillary tension on matrix grain boundaries retains the melt from an ascending buoyant pulse of magma, thus reducing the efficiency of melt extraction. Grain boundary tension also prevents simple gravitational settling of a heavy melt into a thin completely decompacted layer, and gives rise to a thicker boundary layer.

## Acknowledgements

Constructive suggestions by two anonymous reviewers greatly improved the quality of the manuscript. This research was funded by the NSF grant EAR0537599.

## Appendix A. Melt fraction dependence of total interfacial tension

In this section we present a simple 2D micromechanical model relating the total interfacial tension to the melt fraction.

For melt fractions below a critical level,  $\phi_s$ , both solid–solid and solid–liquid interfaces contribute to the total interfacial tension. The schematic diagram in Fig. A.1(a) illustrates the melt distribution on the surface of a control volume, and the shaded region depicts the unit cell for melt fraction less than the disaggregation melt fraction. The total interfacial tension per unit volume  $\chi$  can be expressed as

$$\chi = \sigma_{mm}\alpha_{mm} + \sigma_{mf}\alpha_{mf}, \quad (A.1)$$

where  $\sigma_i$  and  $\alpha_i$  are the interfacial force and interfacial area per unit volume of the interface  $i$ , respectively. The quantity  $\alpha_i$  has the dimension of reciprocal of length, see also [11] for the definition of  $\alpha$ . The semidihedral angle  $\theta$ , subtended by the tangent to the solid–liquid interface to the grain boundary is a material property, related to the ratio of the solid–solid and solid–liquid interfacial tensions, given by

$$\theta = \arccos \frac{\kappa}{2}, \quad (A.2)$$

where  $\kappa = \sigma_{mm}/\sigma_{mf}$ . The melt can reside in the tubules along grain edges for  $0^\circ \leq \theta \leq 90^\circ$  or  $2 \geq \kappa \geq 0$ . For  $\kappa > 2$

or  $\theta < 0^\circ$ , grain boundaries are energetically unstable and are readily wetted by the melt. Eq. (A.2) is a modified form of Young's equation, see [9,10] for a more detailed derivation. The volume fraction of melt can be expressed as a function of the radius of curvature  $r$  of the solid–liquid interface and the semidiheral angle  $\theta$  as

$$\phi = \left(\frac{r}{a}\right)^2 \left(\cos^2\theta - \sin\theta\cos\theta - \frac{\pi}{4} + \theta\right), \quad (\text{A.3})$$

where  $a$  is the size of the unit cell, which is one-fourth of the average grain size. It is also possible to express  $\alpha_i$  as a function of  $r$ ,  $\theta$ , and  $a$ , and using the relation given in Eq. (A.3), as a function of  $\phi$ . The expressions for  $\alpha_i$  become,

$$\alpha_{mf} = \alpha_0 \chi_1 \sqrt{\phi}, \quad (\text{A.4})$$

and

$$\alpha_{mm} = \alpha_0 \left(1 - \chi_2 \sqrt{\phi}\right), \quad (\text{A.5})$$

where  $\alpha_0 = 1/a$  is the volume fraction of grain boundary or solid–solid surface area at  $\phi=0$ , and the constants  $\chi_1$  and  $\chi_2$  are given in Eqs. (A.7) and (A.8). The expressions in Eqs. (A.4) and (A.5) indicate that the solid–liquid interfacial area increases with an increase in the melt fraction while the solid–solid interfacial area decreases with increasing melt fraction. Finally, we combine Eqs. (A.1), (A.4), and (A.5) to obtain

$$\chi = \alpha_0 \left[ \sigma_{mf} \chi_1 \sqrt{\phi} + \sigma_{mm} (1 - \chi_2 \sqrt{\phi}) \right], \text{ for } \phi < \phi_s \quad (\text{A.6})$$

where

$$\chi_1 = \frac{|\frac{\pi}{2} - 2\theta|}{\sqrt{\cos^2\theta - \sin\theta\cos\theta - \frac{\pi}{4} + \theta}}, \quad (\text{A.7})$$

and

$$\chi_2 = \frac{|\cos\theta - \sin\theta|}{\sqrt{\cos^2\theta - \sin\theta\cos\theta - \frac{\pi}{4} + \theta}}. \quad (\text{A.8})$$

At the disaggregation melt fraction  $\phi_s$ , the grain boundaries are completely wetted, i.e. at  $\phi = \phi_s$ ,  $\alpha_{mm} = 0$  in Eq. (A.5), yielding,

$$\phi_s = \left(\frac{1}{\chi_2}\right)^2. \quad (\text{A.9})$$

At melt fractions greater than the disaggregation melt fraction, evolution of the solid–liquid interfacial area can be described by the area of cylindrical grains shrinking uniformly with increasing melt fraction. The diagram in Fig. A.1(b) indicates that under this situation,

$$\phi = 1 - \frac{\pi}{4} \left(\frac{r}{a}\right)^2, \quad (\text{A.10})$$

while

$$\alpha_{mf} = \alpha_0 \sqrt{\pi(1-\phi)}. \quad (\text{A.11})$$

Plugging Eq. (A.11) back into Eq. (A.1), one obtains

$$\chi = \sigma_{mf} \alpha_0 \sqrt{\pi(1-\phi)} \text{ for } \phi > \phi_s. \quad (\text{A.12})$$

The schematic diagram in Fig. A.1(a) illustrates a case where the curvature of the fluid interface is concave toward the solid grain, indicating  $\theta < \pi/4$ . However, the relations given in Eqs. (A.4) and (A.5) are also valid for  $\theta > \pi/4$ , when the solid–liquid interface is convex towards the solid grain.

## Appendix B. Energy conservation

Following [11,20], the total energy balance for a two-phase aggregate is given by:

$$\frac{\overline{\overline{D}}T}{\rho c} + \frac{\tilde{D}(\xi_i \alpha)}{Dt} = Q - \nabla \cdot \mathbf{q} + \Psi - \Delta P \frac{\tilde{D}\phi}{Dt} + (\sigma\alpha - \xi_i \alpha) \nabla \cdot \tilde{\mathbf{v}}, \quad (\text{B.1})$$

where the material derivatives  $\overline{\overline{D}}/Dt$  and  $\tilde{D}/Dt$  are averaged over the matrix and the fluid material derivatives as defined in [11,20]. The quantity  $\xi_i$  is the energy per unit of the interfacial area of the control volume. We define this quantity as

$$\xi_i = \sigma(\phi, T) - T \frac{\partial \sigma(\phi, T)}{\partial T}, \quad (\text{B.2})$$

where  $\sigma$  is the average surface tension per unit area of the control volume. We also define  $\alpha(\phi)$  as the interfacial area in one unit of the control volume. After some algebra, Eqs. (B.1) and (B.2) can be reduced to,

$$\frac{\overline{\overline{D}}T}{\rho c} - T \frac{\tilde{D}}{Dt} \left( \alpha \frac{\partial \sigma}{\partial T} \right) - \alpha T \frac{\partial \sigma}{\partial T} \nabla \cdot \tilde{\mathbf{v}} = Q - \nabla \cdot \mathbf{q} + \Psi - \left( \Delta P + \frac{\partial(\sigma\alpha)}{\partial \phi} \right) \frac{\tilde{D}\phi}{Dt}. \quad (\text{B.3})$$

The terms on the left hand side of Eq. (B.3) are associated with entropy production.

The mechanical work terms on the right hand side of Eq. (B.3) can be further divided into reversible and irreversible work. The reversible components of mechanical work comprise of work done to deform the interface, to isotropically compact or dilate the matrix, and the work done by the interfacial pressure. Thus, the equation for reversible work becomes [20, Eq. (20)]:

$$\frac{\partial \chi}{\partial \phi} + \Delta P = -\frac{K_0 \mu_m}{\phi(1-\phi)} \frac{D_m \phi}{Dt}, \quad (\text{B.4})$$

where we have defined  $\chi = \sigma \alpha$ . In the absence of compaction  $(D_m \phi)/(Dt) = 0$ , Eq. (B.4) represents the Laplace condition. The implication, therefore, is that compaction or dilation is locally controlled by a departure from the Laplace condition.

### Appendix C. Analytical solution

The velocity  $c$  of an individual solitary wave can be calculated analytically as a function of the background melt fraction  $\Phi_0$  and the amplitude  $\Phi_m$  using the method of characteristic variable [3], given by,

$$c = \left( \frac{3R}{4} \right) \left( \frac{\Phi_1 + \Phi_0^2(1-\Phi_0)^2 \Phi_3}{\Phi_0 \Phi_3 - \Phi_2} \right) \quad (\text{C.1})$$

where the functions  $\Phi_1$ ,  $\Phi_2$ , and  $\Phi_3$  depend on  $\Phi_0$  and  $\Phi_m$ , and are given by

$$\begin{aligned} \Phi_1 &= \left( \Phi_m - \Phi_0 + \ln \left( \frac{\Phi_m}{\Phi_0} \right) \right), \\ \Phi_2 &= \left( \frac{1}{\Phi_m^2} - \frac{1}{\Phi_0^2} \right) \\ &\quad - \left[ 2 \left( \frac{1}{1-\Phi_m} - \frac{1}{1-\Phi_0} \right) + 3 \ln \left( \frac{(1-\Phi_0)\Phi_m}{(1-\Phi_m)\Phi_0} \right) \right] \\ \Phi_3 &= \frac{1}{2} \left( \frac{1}{\Phi_m^2} - \frac{1}{\Phi_0^2} \right) + 3 \left( \frac{1}{\Phi_m} - \frac{1}{\Phi_0} \right) \\ &\quad - \left[ 2 \left( \frac{1}{1-\Phi_m} - \frac{1}{1-\Phi_0} \right) + 5 \ln \left( \frac{(1-\Phi_0)\Phi_m}{(1-\Phi_m)\Phi_0} \right) \right]. \end{aligned} \quad (\text{C.2})$$

Stable, real solitary wave solutions are permitted only over a range of possible combinations of the

background and peak melt fractions. The shaded area in the map in Fig. C.1 illustrates the domain of real solitary wave solution to Eqs. (15) and (16). The velocities of the solitary waves in the two possible branches of solution domain are opposite in sign. The analytical solutions were used as initial conditions to the numerical results presented in Section 3.2.2.

### References

- [1] G. Hirth, D.L. Kohlstedt, Experimental constraints on the dynamics of the partially molten upper mantle; deformation in the diffusion creep regime, *J. Geophys. Res., B, Solid Earth Planets* 100 (2) (1995) 1981–2001.
- [2] A. Jellinek, M. Manga, Links between long-lived hotspots, mantle plumes  $D''$ , and plate tectonics, *Rev. Geophys.* 42 (2004) (RG3002).
- [3] M. Rabinowicz, Y. Ricard, M. Grégoire, Compaction in a mantle with a very small melt concentration: implications for the generation of carbonatitic and carbonate-bearing high alkaline mafic melt impregnations, *Earth Planet. Sci. Lett.* 203 (2002) 205–220.
- [4] A. Gudmundsson, Dynamics of volcanic systems in Iceland: example of tectonism and volcanism at juxtaposed hot spot and mid-ocean ridge systems, *Annu. Rev. Earth Planet. Sci.* 28 (2000) 107–140.
- [5] M. Spiegelman, D. McKenzie, Simple 2-D models for melt extraction at mid-ocean ridges and island arcs, *Earth Planet. Sci. Lett.* 83 (1987) 137–152.
- [6] S. Hier-Majumder, D. Kohlstedt, Role of dynamic grain boundary wetting in fluid circulation beneath volcanic arcs, *Geophys. Res. Lett.* 33 (2006) L08305.
- [7] P.J. Wray, The geometry of two-phase aggregates in which the shape of the second phase is determined by its dihedral angle, *Acta Metall.* 24 (1976) 125–135.
- [8] N. von Bargen, H. Waff, Permeabilities, interfacial areas and curvatures of partially molten systems: results of numerical computations of equilibrium microstructures, *J. Geophys. Res.* 91 (1986) 9261–9276.
- [9] F.C. Goodrich, The thermodynamics of fluid interfaces, in: E. Matijević (Ed.), *Surface and Colloid Science*, Wiley-Interscience, New York, 1969, pp. 33–37.
- [10] R.E. Johnson Jr., Conflicts between Gibbsian thermodynamics and recent treatments of interfacial energies in solid–liquid–vapor systems, *J. Phys. Chem.* 63 (10) (1959) 1655–1658.
- [11] D. Bercovici, Y. Ricard, G. Schubert, A two-phase model for compaction and damage; 1, General theory, *J. Geophys. Res., B, Solid Earth Planets* 106 (5) (2001) 8887–8906.
- [12] Y. Ricard, D. Bercovici, G. Schubert, A two-phase model for compaction and damage; 2, Applications to compaction, deformation, and the role of interfacial surface tension, *J. Geophys. Res., B, Solid Earth Planets* 106 (5) (2001).
- [13] D. Bercovici, Y. Ricard, G. Schubert, A two-phase model for compaction and damage; 3, Applications to shear localization and plate boundary formation, *J. Geophys. Res., B, Solid Earth Planets* 106 (5) (2001) 8925–8939.
- [14] D. Stevenson, On the role of surface tension in the migration of melts and fluids, *Geophys. Res. Lett.* 13 (1986) 1149–1152.
- [15] G. Riley, D. Kohlstedt, F. Richter, Melt migration in a silicate liquid–olivine system: an experimental test of compaction theory, *Geophys. Res. Lett.* 17 (1990) 2101–2104.
- [16] G. Riley, D. Kohlstedt, Kinetics of melt migration in upper mantle-type rocks, *Earth Planet. Sci. Lett.* 105 (1991) 500–521.

- [17] K. Mibe, T. Fujii, A. Yasuda, Connectivity of aqueous fluid in earth's upper mantle, *Geophys. Res. Lett.* 25 (8) (1998) 1233–1236.
- [18] E.B. Watson, J.M. Brenan, Fluids in the lithosphere, 1. Experimentally determined wetting characteristics of CO<sub>2</sub>–H<sub>2</sub>O fluids and their implication for fluid transport, host-rock physical properties, and fluid inclusion formation, *Earth Planet. Sci. Lett.* 85 (1987) 497–515.
- [19] Šrámek, Y. Ricard, D. Bercovici, Simultaneous melting and compaction in deformable two-phase media, submitted for publication to *Geophys. J. Int.* (in press).
- [20] D. Bercovici, Y. Ricard, Energetics of two-phase model of lithospheric damage, shear localization and plate-boundary formation, *Geophys. J. Int.* 152 (3) (2003) 581–596.
- [21] W. Kingery, Densification during sintering in the presence of a liquid phase. I: Theory, *J. Appl. Phys.* 30 (3) (1959) 301–306.
- [22] S.-j.L. Kang, *Sintering: Densification, Grain Growth and Microstructure*, Elsevier, 2005.
- [23] J.N. Israelachvili, *Intermolecular and Surface Forces*, 2nd ed., Academic Press, 1991.
- [24] N. Chen, T. Kuhl, R. Tadmor, Q. Lin, J. Israelachvili, Large deformation during coalescence of fluid interfaces, *Phys. Rev. Lett.* 92 (2).
- [25] D. Turcotte, G. Schubert, *Geodynamics*, John Wiley & Sons, 1999.
- [26] R. Cooper, D. Kohlstedt, Interfacial energies in the olivine–basalt system, in: S. Akimoto, M. Manghni (Eds.), *High Pressure Research in Geophysics*, . *Adv. Earth Planet Sci.*, vol. 12, Center for Academic Publications, 1982, pp. 217–228.
- [27] D. Scott, D. Stevenson, Magma ascent by porous flow, *J. Geophys. Res.* 91 (1986) 9283–9296.
- [28] D. Scott, D. Stevenson, Magma solitons, *Geophys. Res. Lett.* 11 (1984) 1161–1164.
- [29] D. Scott, The competition between percolation and circulation in a deformable porous medium, *J. Geophys. Res.* 93 (1988) 6451–6462.
- [30] M. Spiegelman, Flow in deformable porous media, part 2, numerical analysis—the relationship between shock waves and solitary waves, *J. Fluid Mech.* 247 (1993) 39–63.
- [31] V. Barcion, F. Richter, Nonlinear waves in compacting media, *J. Fluid Mech.* 164 (1986) 429–448.
- [32] E. Garnero, J. Revenaugh, Q. Williams, T. Lay, L. Kellogg, The core–mantle boundary region, Ch. *Ultralow Velocity Zones at the Core–Mantle Boundary*, AGU, 1998, pp. 319–334.
- [33] J. Revenaugh, S. Sipkin, Seismic evidence for silicate melt atop the 410-km mantle discontinuity, *Nature* 369 (1994) 474–476.
- [34] E. Ohtani, M. Maeda, Density of basaltic melt at high pressure and stability of the melt at the base of the lower mantle, *Earth Planet. Sci. Lett.* 193 (2001) 69–75.